

Detecting gravitational wave background with equivalent configurations in the network of space based optical lattice clocks

Mingzhi Lou^{1,4,5,*}, Hong Su³, Tao Yang³, and Yun-Long Zhang^{2,1†}

¹*School of Fundamental Physics and Mathematical Sciences,*

Hangzhou Institute for Advanced Study, UCAS, Hangzhou 310024, China

²*National Astronomical Observatories, Chinese Academy of Sciences, Beijing 100101, China*

³*School of Physics and Technology, Wuhan University, Wuhan 430072, China*

⁴*CAS Key Laboratory of Theoretical Physics, Institute of Theoretical Physics, Chinese Academy of Sciences, Beijing 100190, China and*

⁵*Taiji Laboratory for Gravitational Wave Universe (Beijing/Hangzhou), University of Chinese Academy of Sciences, Beijing 100049, China*

The network of space based optical lattice clocks (OLCs) has been proposed to detect the stochastic gravitational wave background. We investigate the overlap reduction function (ORF) of the OLC detector network and analytically derive a transformation that leaves the ORF invariant. This transformation is applicable to configurations with two OLC detectors, each equipped with a one-way link. It can map a configuration with small separation and high noise correlation to another configuration with larger separation and reduced noise correlation. Using this transformation, we obtain a favorable OLC detector network configuration with high cross-correlation response, and compare its sensitivity to that of space-based laser interferometer gravitational wave detectors.

CONTENTS

I. Introduction	1
II. Overlap reduction function	2
III. Equivalent configurations	2
A. Nontrivial solutions	3
IV. Application for the GW detection	3
A. Response function	4
B. Sensitivity curves	4
V. Conclusion and discussion	6
Acknowledgments	7
References	7

I. INTRODUCTION

Since the first direct observation of the gravitational wave from the binary black hole merger by LIGO in 2015 [1], ground-based detectors have detected dozens of compact binary coalescences, profoundly enhancing our understanding of compact objects like black holes and neutron stars [2–4]. However, due to limitations from arm length and seismic noise in LIGO [5], Virgo [6], and KAGRA [7], the sensitive band of terrestrial detectors is mainly above 10 Hz [8]. To detect low frequency gravitational waves in the millihertz range, space-based detectors are required. The LISA mission is one of the

space-based laser interferometric gravitational-wave detectors, which will be sensitive in the 0.1 mHz to 0.1 Hz band [9]. Concurrently, the Taiji [10] and TianQin [11] programs aim to explore the low-frequency gravitational-wave universe with similar architectures. In the even lower nanohertz frequency band, Pulsar Timing Arrays (PTAs) [12] utilize the timing signals from an array of millisecond pulsars to detect GWs from the cosmic population of supermassive black hole binaries [13], and have reported evidence for a background signal [14–17].

In recent years, gravitational-wave detection schemes based on optical lattice clocks (OLCs) have been proposed as a newly emerging technology, demonstrating great potential [18, 19]. Indeed, OLCs possess exceptional stability and precision [20, 21]. By comparing the frequency variations of optical signals between two spatially separated OLCs, it is possible to sense spacetime perturbations caused by passing gravitational waves [22]. One of the core scientific objectives in gravitational wave cosmology [23] is the stochastic gravitational wave background (SGWB). It may originate from physical processes in the early universe [24, 25], such as cosmic strings [26, 27], first-order phase transitions [28, 29], and inflation [30, 31]. It could also arise from the superposition of numerous unresolved astrophysical sources [32, 33]. Detecting the SGWB is of fundamental importance for understanding the very early history of the universe, fundamental physical laws, and the evolution of massive black holes.

One of the most effective methods for detecting the SGWB is to use multiple detectors for cross-correlation analysis [34, 35]. This method correlates the data streams from different detectors, effectively suppressing correlated instrumental noise and thereby extracting weak, common gravitational-wave signals. Applying the cross-correlation method to data from two OLC detectors can significantly enhance the sensitivity for detect-

* loumingzhi23@mails.ucas.ac.cn

† zhangyunlong@nao.cas.cn

ing the SGWB [36]. The sensitivity of a detector network depends on the detector noise as well as the cross-correlation response. The cross-correlation response is fundamentally determined by the geometric factors of a detector pair, including their relative distance and orientation. The cross-correlation response function of a detector network, sometimes referred to as the overlap reduction function (ORF), is used to quantify these geometric factors. This function is defined as the sky-integrated average of the product of the two detectors' response functions. Currently, analytical expressions for precisely calculating the ORF have been derived in previous work [37, 38]. However, research on how to find the optimal geometric configuration for an OLC detector network that yields high response and effectively suppresses local noise remains an area of active investigation and presents significant challenges [36].

In this paper, we aim to investigate the transformation relationships among OLC detector network configurations with equal cross-correlation responses. Through analytical methods, we derive a non-trivial transformation and analyze its geometric implications. This transformation can convert a configuration with small separation, high cross-correlation response, but also high noise correlation into another configuration with larger separation and lower noise correlation. This discovery provides new theoretical tools and design ideas for optimizing the layout of OLC detector networks.

The structure of this paper is as follows: In Sec. II, we review the fundamental theory of the overlap reduction functions of OLC network. In Sec. III, we detail the transformation relationships among OLC detector network configurations with equal cross-correlation responses, including both trivial and non-trivial solutions, and provide the specific construction method. In Sec. IV, we discuss the properties under equal arm lengths and apply the constructed configuration to a realistic orbital scenario, comparing its sensitivity with that of LISA, Taiji, and TianQin. In Sec. V, we summarize the work and discuss the results.

II. OVERLAP REDUCTION FUNCTION

A single OLC detector can be regarded as a system composed of two satellites and a single one-way laser link. The geometric configuration of a single OLC detector can be described by three parameters: the position of the end point \vec{x}_i , the arm length L_i , and the direction vector \hat{u}_i , collectively denoted as $\{\vec{x}_i, L_i \hat{u}_i\}$. Similarly, the configuration of two OLC detectors is defined by $\{\vec{x}_1, L_1 \hat{u}_1, \vec{x}_2, L_2 \hat{u}_2\}$. Fig. 1 schematically illustrates the configuration for calculating the cross-correlation response of an OLC detector pair.

The ORF in this paper refers to the response of two OLC detectors to SGWB, defined as the inner product of the two OLC detectors' response functions. The ORF

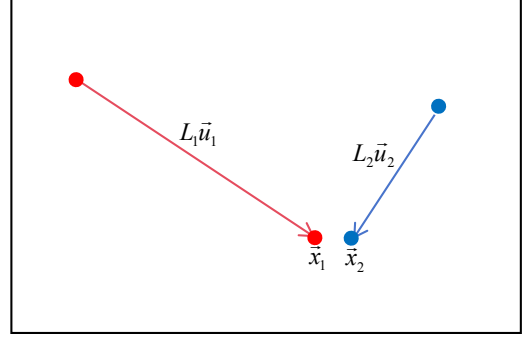


FIG. 1: The cross-correlation configuration between OLC detector 1 (red) and OLC detector 2 (blue). Each OLC detector consists of a single laser link connecting two satellites.

for a pair of OLC detectors is [34]

$$\mathcal{R}_{12}(f) = \sum_{\lambda=+,\times} \int \frac{d^2 \hat{n}}{4\pi} F_1^\lambda(\hat{n}, f) F_2^{\lambda*}(\hat{n}, f) e^{-i \frac{2\pi f}{c} \hat{n} \cdot \vec{x}_{12}}, \quad (1)$$

where $\vec{x}_{12} = \vec{x}_1 - \vec{x}_2$, \vec{x}_i is the position of the laser link endpoint on the respective detector i , and \hat{n} is a unit vector in the direction of GW propagation.

For an OLC detector i , the pattern function

$$F_i^\lambda(\hat{n}, f) = \frac{1}{2} u_i^a u_i^b \epsilon_{ab}^\lambda(\hat{n}) \mathcal{T}_i(\hat{n} \cdot \hat{u}_i, f), \quad (2)$$

where $\epsilon_{ab}^\lambda(\hat{n})$ is the polarization tensor for gravitational-wave polarization mode A , u_i^a is the respective unit vector of the laser propagation direction, and $\mathcal{T}(\hat{n} \cdot \hat{u}_i, f)$ is the transfer function

$$\mathcal{T}_i(\hat{n} \cdot \hat{u}_i, f) = i \frac{2\pi f L_i}{c} \text{sinc} \left[\frac{\pi f L_i}{c} (1 - \hat{n} \cdot \hat{u}_i) \right] e^{-i \frac{\pi f L_i}{c} (1 - \hat{n} \cdot \hat{u}_i)}. \quad (3)$$

Here, L_i is the arm length of the OLC detector i , and \hat{u}_i is the unit vector along its laser propagation direction.

III. EQUIVALENT CONFIGURATIONS

For a given OLC detector network configuration $\{\vec{x}_1, L_1 \hat{u}_1, \vec{x}_2, L_2 \hat{u}_2\}$, we aim to identify another OLC detector network configuration $\{\vec{x}_3, L_3 \hat{u}_3, \vec{x}_4, L_4 \hat{u}_4\}$ such that their response magnitude satisfies

$$|\mathcal{R}_{12}(f)| = |\mathcal{R}_{34}(f)|. \quad (4)$$

We can easily identify two types of solutions: The first type of solution, $\{\vec{x}_1 + \vec{a}, L_1 \hat{u}_1, \vec{x}_2 + \vec{a}, L_2 \hat{u}_2\}$, is generated by translating the original configuration $\{\vec{x}_1, L_1 \hat{u}_1, \vec{x}_2, L_2 \hat{u}_2\}$ by vector \vec{a} . The second type of solution, $\{\hat{O}\vec{x}_1, L_1 \hat{O}\hat{u}_1, \hat{O}\vec{x}_2, L_2 \hat{O}\hat{u}_2\}$, is generated from the original configuration $\{\vec{x}_1, L_1 \hat{u}_1, \vec{x}_2, L_2 \hat{u}_2\}$ via an orthogonal transformation \hat{O} . However, these two types of

solutions do not correspond to non-trivial configurations, as they preserve both the relative separation and the mutual angular relationships of the original configuration.

A. Nontrivial solutions

To identify solutions corresponding to non-trivial configurations, we reformulate the ORF of Eq. (1) in the following form:

$$\begin{aligned} \mathcal{R}_{12}(f) = & \sum_{\lambda} \int \frac{d^2 \hat{n}}{4\pi} u_1^a u_1^b \epsilon_{ab}^{\lambda}(\hat{n}) u_2^c u_2^d \epsilon_{cd}^{\lambda}(\hat{n}) \\ & \times \text{sinc}\left[\frac{\pi f L_1}{c}(1 - \hat{u}_1 \cdot \hat{n})\right] \text{sinc}\left[\frac{\pi f L_2}{c}(1 - \hat{u}_2 \cdot \hat{n})\right] \\ & \times L_1 L_2 \left(\frac{\pi f}{c}\right)^2 e^{-i\alpha_{12}} e^{-i\beta_{12}}, \end{aligned} \quad (5)$$

where $\alpha_{12} = 2\pi f \left(\frac{L_1}{2} \hat{u}_1 - \frac{L_2}{2} \hat{u}_2 + \vec{x}_1 - \vec{x}_2\right) \cdot \hat{n}/c$, and $\beta_{12} = \pi f (L_2 - L_1)/c$.

To find the solutions satisfying Eq. (4), our strategy here is to allow the integrand of $\mathcal{R}_{12}(f)$ to differ from that of $\mathcal{R}_{34}(f)$ via an overall $O(2)$ transformation in the complex plane. According to Eq. (5), we find that the factors preceding the exponential factor are real-valued. Hence, we first equate these real factors for $\mathcal{R}_{12}(f)$ and $\mathcal{R}_{34}(f)$, which readily yields two conditions:

$$L_3 = L_2, \hat{u}_3 = \hat{u}_2, L_4 = L_1, \hat{u}_4 = \hat{u}_1, \quad (6)$$

$$L_3 = L_1, \hat{u}_3 = \hat{u}_1, L_4 = L_2, \hat{u}_4 = \hat{u}_2. \quad (7)$$

Substituting these two conditions into the exponential factors yields the corresponding solutions, respectively. For convenience, we denote the original configuration as configuration {A}.

When Eq. (6) is adopted as a condition, we have $\beta_{12} = -\beta_{34}$, two subcases arise. First, if $\alpha_{12} = \alpha_{34}$, then

$$(\vec{x}_1 + L_1 \hat{u}_1) - (\vec{x}_2 + L_2 \hat{u}_2) = \vec{x}_3 - \vec{x}_4, \quad (8)$$

and the resulting configuration is $\{\vec{x}_1 + L_1 \hat{u}_1, L_2 \hat{u}_2, \vec{x}_2 + L_2 \hat{u}_2, L_1 \hat{u}_1\}$, which we label as configuration {B} (corresponding to detectors 3 and 4 in Fig. 2). Second, if $\alpha_{12} = -\alpha_{34}$, then

$$\vec{x}_1 - \vec{x}_2 = \vec{x}_4 - \vec{x}_3, \quad (9)$$

and the resulting configuration is $\{\vec{x}_2, L_2 \hat{u}_2, \vec{x}_1, L_1 \hat{u}_1\}$. This is essentially the original configuration {A} with the labels 1 and 2 swapped.

When Eq. (7) is adopted as a condition, we have $\beta_{12} = \beta_{34}$, and again two subcases arise. First, if $\alpha_{12} = \alpha_{34}$, then

$$\vec{x}_1 - \vec{x}_2 = \vec{x}_3 - \vec{x}_4, \quad (10)$$

and the resulting configuration is $\{\vec{x}_1 + \vec{a}, L_1 \hat{u}_1, \vec{x}_2 + \vec{a}, L_2 \hat{u}_2\}$, which is identical to the original configuration {A} (a pure translation). Second, if $\alpha_{12} = -\alpha_{34}$, then

$$(\vec{x}_1 + L_1 \hat{u}_1) - (\vec{x}_2 + L_2 \hat{u}_2) = \vec{x}_4 - \vec{x}_3, \quad (11)$$

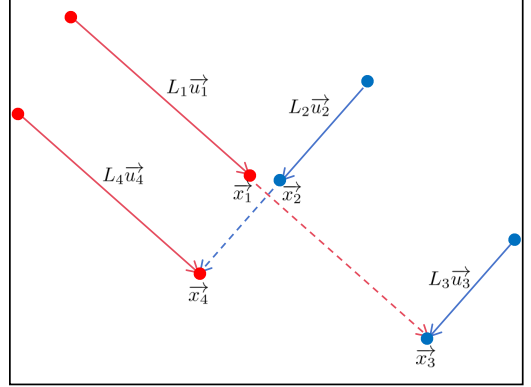


FIG. 2: A non-trivial transformation that leaves the ORF invariant. The original configuration {A} (Detectors 1 & 2) transforms into the new configuration {B} (Detectors 3 & 4). Here, detector i is $\{\vec{x}_i, L_i \hat{u}_i\}$, solid arrows indicate laser links, and dashed arrows represent auxiliary lines.

and the resulting configuration is $\{\vec{x}_2 + L_2 \hat{u}_2, L_1 \hat{u}_1, \vec{x}_1 + L_1 \hat{u}_1, L_2 \hat{u}_2\}$. We label this configuration as configuration {C}, which can be obtained by exchanging the labels 3 and 4 in configuration {B} (see Fig. 2).

As discussed above, we obtain a non-trivial solution given by $\{\vec{x}_1 + L_1 \hat{u}_1, L_2 \hat{u}_2, \vec{x}_2 + L_2 \hat{u}_2, L_1 \hat{u}_1\}$, while the complete general solution remains undetermined. Fig. 2 illustrates the construction of the corresponding equivalent configuration {B} from an arbitrary original configuration {A}, as follows:

1). Set $\vec{x}_3 = \vec{x}_1 + L_1 \hat{u}_1$ and $\vec{x}_4 = \vec{x}_2 + L_2 \hat{u}_2$.

2). Following the condition in Eq. (6), copy Link 2 from \vec{x}_2 to \vec{x}_3 to generate Link 3, and copy Link 1 from \vec{x}_1 to \vec{x}_4 to generate Link 4.

Thus, the method allows us to construct a configuration {B} for which the magnitude of the ORF $|\mathcal{R}_{34}(f)|$ matches that of $|\mathcal{R}_{12}(f)|$ for any given configuration {A}. Applying the same method again to configuration {B} recovers the initial configuration {A}, as shown by the following derivation:

$$\begin{aligned} \vec{x}_5 - \vec{x}_6 &= \vec{x}_3 + L_3 \hat{u}_3 - \vec{x}_4 - L_4 \hat{u}_4 \\ &= \vec{x}_1 + L_1 \hat{u}_1 + L_2 \hat{u}_2 - \vec{x}_2 - L_2 \hat{u}_2 - L_1 \hat{u}_1 \\ &= \vec{x}_1 - \vec{x}_2. \end{aligned} \quad (12)$$

IV. APPLICATION FOR THE GW DETECTION

In general, the method presented in the previous section is applicable to configurations consisting of two OLC detectors, each equipped with a single one-way link. Furthermore, if $L_1 = L_2$, then $\beta_{12} = \beta_{34} = 0$. For configuration {B} with $\alpha_{12} = \alpha_{34}$, the real and imaginary parts of $\mathcal{R}_{12}(f)$ and $\mathcal{R}_{34}(f)$ are all equal, so $\mathcal{R}_{12}(f) = \mathcal{R}_{34}(f)$. In practical data analysis, the real and imaginary parts of the cross-correlation response are often used instead of its

modulus. Therefore, the construction method described above is particularly convenient when the arm lengths are equal. In the following, we focus on the case where the two detectors have equal arm lengths, i.e., $L_1 = L_2 = L$.

A. Response function

In most cases, one configuration of a pair of OLC detectors is compact, while its equivalent configuration is more widely separated. For instance, in Fig. 2, detectors (3 & 4) are farther apart than detectors (1 & 2). Fig. 3 illustrates a more extreme case: in configuration (a), \vec{x}_1 and \vec{x}_2 coincide, while in its equivalent configuration (b), \vec{x}_3 and \vec{x}_4 are separated by a distance of $2L\sin(\theta/2)$.

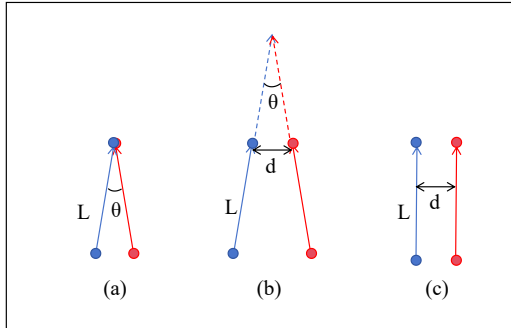


FIG. 3: Three types of detector configurations: (a) denotes two links sharing a common endpoint with an included angle θ ; (b) denotes the configuration that is equivalent to (a), where the distance between the link endpoints is $d = 2L\sin(\theta/2)$; (c) denotes the configuration with two parallel links separated by the same distance d .

It is noteworthy that this method can transform the closely-spaced OLC detector network configurations (1 & 2) into widely-spaced ones (3 & 4) with identical cross-correlation responses, thereby reducing the correlation of local noise. Moreover, when detectors 1 & 2 are in close proximity, the magnitude of $\mathcal{R}_{12}(f)$ is generally higher. Therefore, the transformed OLC detector network (3 & 4) combines the advantages of a high cross-correlation response and low noise correlation. In fact, the OLC detector network configuration (a) shown in Fig. 3 closely resembles the simplified PTA configuration. Thus, we can refer to the Hellings-Downs curve [39] when selecting the angle between two OLC detectors.

In Fig. 4, we compare the cross-correlation responses of configurations (b) and (c) from Fig. 3, based on their response magnitudes. Furthermore, it can be proven that the imaginary parts are zero in both cases. For configuration (b), the angle between the two links is set to 20° , while for configuration (c), the two links are parallel. As a result, the response of configuration (c) is slightly superior to that of configuration (b) in the low-frequency band. By contrast, configuration (b) exhibits a super-

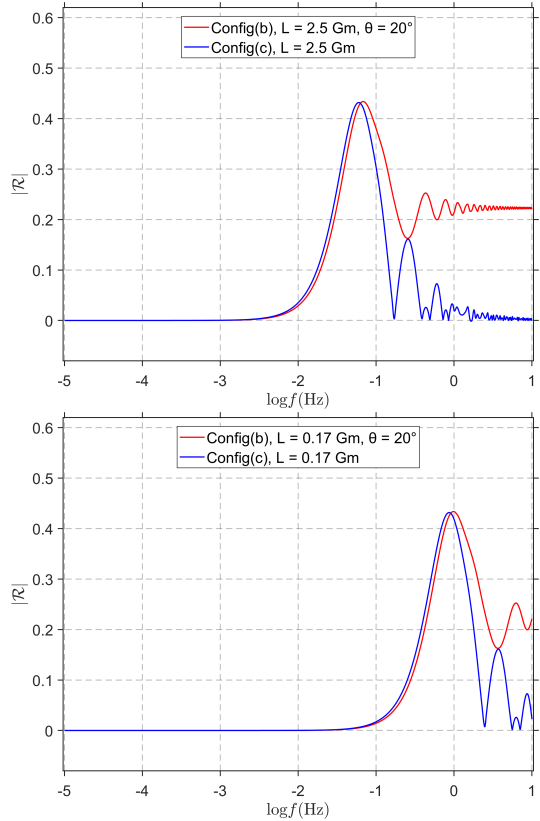


FIG. 4: The ORFs of the two types of configurations (b) and (c) in Fig. 3 are plotted based on Eq. (5), with $\theta = 20^\circ$, $L = 2.5 \text{ Gm}$ and 0.17 Gm , respectively.

rior response to configuration (c) in the high-frequency band. Overall, configuration (b) demonstrates a better cross-correlation response. Therefore, when the separation between two sets of OLC detectors remains fixed, a smaller angle between their baselines does not necessarily yield a better cross-correlation response.

B. Sensitivity curves

The effective strain noise of the OLC detector network can be written as [36]:

$$\tilde{h}_{12}(f) = \left[(\tau \Delta f) \left(\frac{\mathcal{R}_n^2(f)}{N_{\text{total}}^2(f)} \right) \right]^{-1/4}, \quad (13)$$

where $\overline{X(f)}$ denotes the average of $X(f)$ over a small interval centered at f with width Δf , and τ is the observation time. We adopt $\tau = 1$ year and frequency resolution $\Delta f = f/10$, as in Ref. [36].

The total noise power spectral density for the OLC detector comprises three main contributions: quantum projection noise (QPN), photon shot noise (PSN), and acceleration noise (AN): $N_{\text{total}}(f) = N_{\text{QPN}}(f) + N_{\text{PSN}}(f) +$

$N_{\text{AN}}(f)$, where

$$N_{\text{QPN}}(f) = \frac{2}{(2\pi\nu)^2 NT}, \quad (14)$$

$$N_{\text{PSN}}(f) = \frac{2f^2 \Delta_L}{\nu^2 [(2\pi f)^2 + \eta P_L \Delta_L / (2\pi \hbar \nu)]}, \quad (15)$$

$$N_{\text{AN}}(f) = \frac{S_L}{c^2 (2\pi f)^2}. \quad (16)$$

Here, we choose the parameter values as in Ref. [22],

$$\nu = 430 \text{ THz}, \quad N = 7 \times 10^6, \quad T = 160 \text{ s}, \quad \eta = 0.5, \\ \Delta_L = 30 \text{ mHz}, \quad P_L = 3 \text{ pW}, \quad S_L = 9 \text{ fm}^2 \text{ s}^{-4} \text{ Hz}^{-1}. \quad (17)$$

It has been demonstrated that points located near the center of a circle with radius R in a plane inclined at 60° to the ecliptic can maintain relative stationarity, provided the orbital eccentricity remains small [40]. In Fig. 5, we show the configuration (b) placed on a circle of radius R with an inclination of 60° relative to the ecliptic plane. Here, the angle θ is set to 21.78° , which is derived from the relation $L = \sqrt{3}R$.

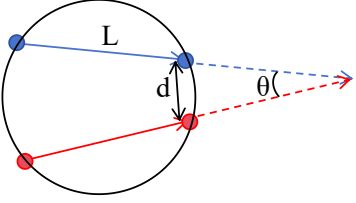


FIG. 5: Schematic of the OLC detector configuration (b) with $\theta = 21.78^\circ$ in a circular formation, which is analogous to LISA's orbital configuration.

In Fig. 6, we compare the effective strain noise of the OLC detector network configuration (b) with that of the space-based laser interferometer gravitational wave detectors: LISA, Taiji, and TianQin. The effective strain noise is given by [41]

$$\tilde{h}_n(f) = \sqrt{\frac{N_m(f)}{\mathcal{R}_m(f)}}. \quad (18)$$

We choose the approximated Michelson-type channel noise model $N_m(f)$ as in [42]

$$N_m(f) = \frac{A_{\text{OMS}}^2}{L^2} \left[1 + \left(\frac{2 \text{ mHz}}{f} \right)^4 \right] + \left[1 + \cos^2 \left(\frac{2\pi f L}{c} \right) \right] \\ \times \frac{2A_{\text{acc}}^2}{(2\pi f)^4 L^2} \left[1 + \left(\frac{0.4 \text{ mHz}}{f} \right)^2 \right] \left[1 + \left(\frac{f}{8 \text{ mHz}} \right)^4 \right]. \quad (19)$$

The noise parameters are summarized in Table I.

The sky averaged response function $\mathcal{R}_m(f)$ is [41]

$$\mathcal{R}_m(f) = \sum_{A=+, \times} \int \frac{d^2 \hat{n}}{4\pi} F_m^\lambda(\hat{n}, f) F_m^{\lambda*}(\hat{n}, f), \quad (20)$$

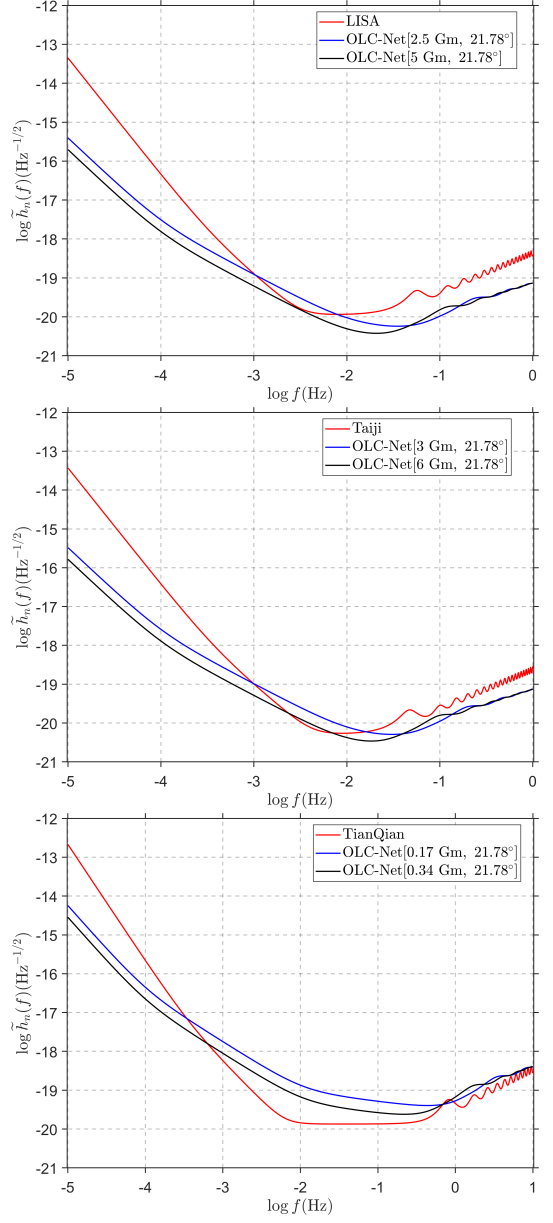


FIG. 6: Comparison of the effective strain noise in Eq. (18) for LISA, Taiji, TianQin, and OLC detector network configuration (b) in Fig. 3. For the OLC network, we use Eq. (13) and two arm lengths are considered: one that matches the triangular detector's arm, the other being twice as long.

Parameters	LISA	Taiji	TianQin
$L(10^9 \text{ m})$	3	2.5	0.17
$A_{\text{OMS}}^2 (\text{pm}^2/\text{Hz})$	225	64	1
$A_{\text{acc}}^2 (\text{fm}^2/\text{s}^4/\text{Hz})$	9	9	1

TABLE I: The noise parameters of LISA [42], Taiji [43], and TianQin [11] are summarized in this table.

where the pattern function

$$F_m^\lambda(\hat{n}, f) = D_m^{ab}(\hat{n}, f) \epsilon_{ab}^\lambda(\hat{n}), \quad (21)$$

the detector response tensor

$$D_m^{ab}(\hat{n}, f) = \frac{1}{2} [u^a u^b \mathcal{T}_m(\hat{u} \cdot \hat{n}, f) - v^a v^b \mathcal{T}_m(\hat{v} \cdot \hat{n}, f)], \quad (22)$$

and the transfer function

$$\mathcal{T}_m(\hat{u} \cdot \hat{n}, f) = \frac{1}{2} \text{sinc}\left[\frac{\pi f L}{c}(1 - \hat{u} \cdot \hat{n})\right] e^{-i\frac{\pi f L}{c}(3 + \hat{u} \cdot \hat{n})} + \frac{1}{2} \text{sinc}\left[\frac{\pi f L}{c}(1 + \hat{u} \cdot \hat{n})\right] e^{-i\frac{\pi f L}{c}(1 + \hat{u} \cdot \hat{n})}. \quad (23)$$

The effective strain noise $\tilde{h}_n(f)$ in Eq. (13) and Eq. (18), can be further converted into the dimensionless gravitational-wave energy density spectrum [41],

$$\Omega_n h^2 = \frac{4\pi^2 f^3}{3(H_0/h)^2} \tilde{h}_n^2(f). \quad (24)$$

Here, H_0 is the present-day Hubble parameter, conventionally written as $H_0 = 100 h \text{ km s}^{-1} \text{ Mpc}^{-1}$. To avoid dependence on the specific value of the dimensionless parameter h , we use $H_0/h \simeq 3.24 \times 10^{-18} \text{ s}^{-1}$, and the results of $\Omega_n h^2$ are plotted in Fig. 7. The OLC detector network configuration (b) demonstrates superior sensitivity to LISA and Taiji in both the low and high frequency bands. For shorter arm length and in the high frequency band, TianQin demonstrates better sensitivity to that of the OLC detector network configuration (b). The medium frequency regime around millihertz corresponds to the most sensitive band for LISA and Taiji, where they achieve relatively superior sensitivity.

V. CONCLUSION AND DISCUSSION

In this paper, we investigate the geometric configurations of OLC detector networks that exhibit equal cross-correlation responses. Using an analytical approach, we derive specific solutions to the equation $|\mathcal{R}_{12}(f)| = |\mathcal{R}_{34}(f)|$ and the geometric relationships corresponding to these solutions. A key result is the identification of a nontrivial geometric transformation, distinct from trivial operations such as translation, rotation, or relabeling. This nontrivial geometric transformation is summarized as the geometric construction method illustrated in Fig. 2. It can alter the distance between the two detectors without changing the magnitude of the cross-correlation response. In particular, when the detectors have equal arm lengths, $\mathcal{R}_{12}(f) = \mathcal{R}_{34}(f)$, where both the real and imaginary parts of the ORFs are equal.

It is noteworthy that this method can transform some closely-spaced OLC detector network configurations into equivalent widely-spaced configurations, thereby reducing the correlation of local noise. Therefore, in the practical design of OLC detector networks, we may initially

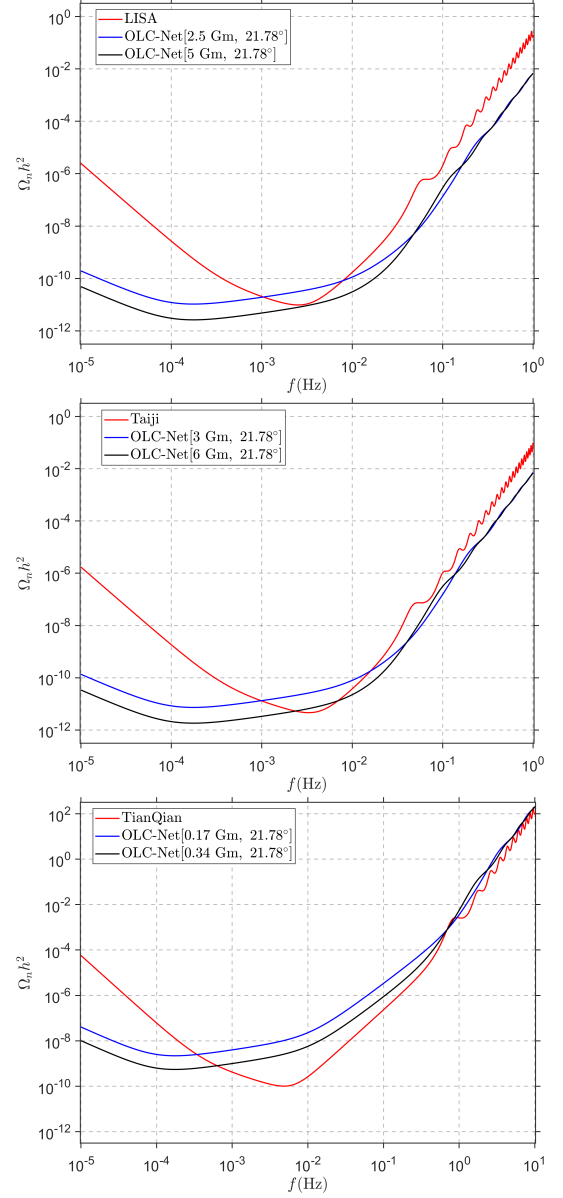


FIG. 7: Sensitivity curves for the total intensity of LISA, Taiji, TianQin and OLC detector network configuration (b) in Fig. 3.

consider some closely-spaced, noise-correlated configurations rather than directly excluding them. In general, this method is applicable to configurations consisting of two OLC detectors with one-way links.

We also apply the aforementioned non-trivial transformation to an OLC configuration analogous to the PTA, converting it into a new OLC configuration. The ORF of this new configuration is compared with that of a parallel configuration with equal arm lengths and equal spacing. The results show that the new configuration exhibits a better response in the high-frequency region, while its low-frequency response remains comparable to that of the parallel configuration. Finally, we place this new

OLC configuration in a realistic orbit and compare its sensitivity with those of LISA, Taiji, and TianQin.

correlation configurations.

ACKNOWLEDGMENTS

Based on the work presented in this paper, several challenges remain to be addressed in the future. For example, we can seek other nontrivial solutions and explore nontrivial transformations that leave the circular polarization components of the ORF unchanged [44, 45]. It is also interesting to build on concepts like those in [37], decompose complex links into constituent one-way links and applying the proposed transformation to their cross-

This work is supported by the National Key Research and Development Program of China (No. 2023YFC2206200, No. 2021YFC2201901), the National Natural Science Foundation of China (No. 12375059, No. 12575063), and the Project of National Astronomical Observatories, Chinese Academy of Sciences (No. E4TG6601). We thank helpful conversation with Bo Wang.

[1] B. P. Abbott *et al.* (LIGO Scientific, Virgo), Observation of Gravitational Waves from a Binary Black Hole Merger, *Phys. Rev. Lett.* **116**, 061102 (2016), arXiv:1602.03837 [gr-qc].

[2] B. P. Abbott *et al.* (LIGO Scientific, Virgo), GW170817: Observation of Gravitational Waves from a Binary Neutron Star Inspiral, *Phys. Rev. Lett.* **119**, 161101 (2017), arXiv:1710.05832 [gr-qc].

[3] B. P. Abbott *et al.* (LIGO Scientific, Virgo), Tests of general relativity with GW150914, *Phys. Rev. Lett.* **116**, 221101 (2016), [Erratum: *Phys. Rev. Lett.* 121, 129902 (2018)], arXiv:1602.03841 [gr-qc].

[4] R. Abbott *et al.* (LIGO Scientific, KAGRA, VIRGO), Observation of Gravitational Waves from Two Neutron Star–Black Hole Coalescences, *Astrophys. J. Lett.* **915**, L5 (2021), arXiv:2106.15163 [astro-ph.HE].

[5] J. Aasi *et al.* (LIGO Scientific), Advanced LIGO, *Class. Quant. Grav.* **32**, 074001 (2015), arXiv:1411.4547 [gr-qc].

[6] F. Acernese *et al.* (VIRGO), Advanced Virgo: a second-generation interferometric gravitational wave detector, *Class. Quant. Grav.* **32**, 024001 (2015), arXiv:1408.3978 [gr-qc].

[7] K. Somiya (KAGRA), Detector configuration of KAGRA: The Japanese cryogenic gravitational-wave detector, *Class. Quant. Grav.* **29**, 124007 (2012), arXiv:1111.7185 [gr-qc].

[8] M. Punturo *et al.*, The Einstein Telescope: A third-generation gravitational wave observatory, *Class. Quant. Grav.* **27**, 194002 (2010).

[9] P. A. Seoane *et al.* (eLISA), The Gravitational Universe, ArXiv (2013), arXiv:1305.5720 [astro-ph.CO].

[10] W.-R. Hu and Y.-L. Wu, The Taiji Program in Space for gravitational wave physics and the nature of gravity, *Natl. Sci. Rev.* **4**, 685 (2017).

[11] J. Luo *et al.* (TianQin), TianQin: a space-borne gravitational wave detector, *Class. Quant. Grav.* **33**, 035010 (2016), arXiv:1512.02076 [astro-ph.IM].

[12] S. L. Detweiler, Pulsar timing measurements and the search for gravitational waves, *Astrophys. J.* **234**, 1100 (1979).

[13] S. Burke-Spolaor *et al.*, The Astrophysics of Nanohertz Gravitational Waves, *Astron. Astrophys. Rev.* **27**, 5 (2019), arXiv:1811.08826 [astro-ph.HE].

[14] Z. Arzoumanian *et al.* (NANOGrav), The NANOGrav 12.5 yr Data Set: Search for an Isotropic Stochastic Gravitational-wave Background, *Astrophys. J. Lett.* **905**, L34 (2020), arXiv:2009.04496 [astro-ph.HE].

[15] B. Goncharov *et al.*, On the Evidence for a Common-spectrum Process in the Search for the Nanohertz Gravitational-wave Background with the Parkes Pulsar Timing Array, *Astrophys. J. Lett.* **917**, L19 (2021), arXiv:2107.12112 [astro-ph.HE].

[16] S. Chen *et al.* (EPTA), Common-red-signal analysis with 24-yr high-precision timing of the European Pulsar Timing Array: inferences in the stochastic gravitational-wave background search, *Mon. Not. Roy. Astron. Soc.* **508**, 4970 (2021), arXiv:2110.13184 [astro-ph.HE].

[17] J. Antoniadis *et al.*, The International Pulsar Timing Array second data release: Search for an isotropic gravitational wave background, *Mon. Not. Roy. Astron. Soc.* **510**, 4873 (2022), arXiv:2201.03980 [astro-ph.HE].

[18] F. He and B. Zhang, A protocol of potential advantage in the low frequency range to gravitational wave detection with space based optical atomic clocks, *Eur. Phys. J. D* **74**, 94 (2020), arXiv:2005.06817 [gr-qc].

[19] T. Ebisuzaki, H. Katori, J. Makino, A. Noda, H. Shinkai, and T. Tamagawa, INO: Interplanetary Network of Optical Lattice Clocks, *Int. J. Mod. Phys. D* **29**, 1940002 (2019), arXiv:1809.10317 [astro-ph.IM].

[20] N. Hinkley, J. A. Sherman, N. B. Phillips, M. Schioppo, N. D. Lemke, K. Belyov, M. Pizzocaro, C. W. Oates, and A. D. Ludlow, An Atomic Clock with 10^{-18} Instability, *Science* **341**, 1215 (2013), arXiv:1305.5869 [physics.atom-ph].

[21] B. J. Bloom, T. L. Nicholson, J. R. Williams, S. L. Campbell, M. Bishof, X. Zhang, W. Zhang, S. L. Bromley, and J. Ye, An Optical Lattice Clock with Accuracy and Stability at the 10^{-18} Level, *Nature* **506**, 71 (2014), arXiv:1309.1137 [physics.atom-ph].

[22] S. Kolkowitz, I. Pikovski, N. Langellier, M. D. Lukin, R. L. Walsworth, and J. Ye, Gravitational wave detection with optical lattice atomic clocks, *Phys. Rev. D* **94**, 124043 (2016), arXiv:1606.01859 [physics.atom-ph].

[23] N. Christensen, Stochastic Gravitational Wave Backgrounds, *Rept. Prog. Phys.* **82**, 016903 (2019), arXiv:1811.08797 [gr-qc].

[24] M. Maggiore, Gravitational wave experiments and early universe cosmology, *Phys. Rept.* **331**, 283 (2000), arXiv:gr-qc/9909001.

[25] C. Caprini and D. G. Figueroa, Cosmological Back-

grounds of Gravitational Waves, *Class. Quant. Grav.* **35**, 163001 (2018), arXiv:1801.04268 [astro-ph.CO].

[26] T. Damour and A. Vilenkin, Gravitational wave bursts from cusps and kinks on cosmic strings, *Phys. Rev. D* **64**, 064008 (2001), arXiv:gr-qc/0104026.

[27] X. Siemens, V. Mandic, and J. Creighton, Gravitational wave stochastic background from cosmic (super)strings, *Phys. Rev. Lett.* **98**, 111101 (2007), arXiv:astro-ph/0610920.

[28] E. Witten, Cosmic Separation of Phases, *Phys. Rev. D* **30**, 272 (1984).

[29] M. Kamionkowski, A. Kosowsky, and M. S. Turner, Gravitational radiation from first order phase transitions, *Phys. Rev. D* **49**, 2837 (1994), arXiv:astro-ph/9310044.

[30] V. F. Mukhanov, H. A. Feldman, and R. H. Brandenberger, Theory of cosmological perturbations. Part 1. Classical perturbations. Part 2. Quantum theory of perturbations. Part 3. Extensions, *Phys. Rept.* **215**, 203 (1992).

[31] M. S. Turner, Detectability of inflation produced gravitational waves, *Phys. Rev. D* **55**, R435 (1997), arXiv:astro-ph/9607066.

[32] A. J. Farmer and E. S. Phinney, The gravitational wave background from cosmological compact binaries, *Mon. Not. Roy. Astron. Soc.* **346**, 1197 (2003), arXiv:astro-ph/0304393.

[33] S. R. Taylor and J. R. Gair, Cosmology with the lights off: standard sirens in the Einstein Telescope era, *Phys. Rev. D* **86**, 023502 (2012), arXiv:1204.6739 [astro-ph.CO].

[34] B. Allen and J. D. Romano, Detecting a stochastic background of gravitational radiation: Signal processing strategies and sensitivities, *Phys. Rev. D* **59**, 102001 (1999), arXiv:gr-qc/9710117.

[35] E. Thrane and J. D. Romano, Sensitivity curves for searches for gravitational-wave backgrounds, *Phys. Rev. D* **88**, 124032 (2013), arXiv:1310.5300 [astro-ph.IM].

[36] B. Wang, B. Li, Q. Xiao, G. Mo, and Y.-F. Cai, Space-based optical lattice clocks as gravitational wave detectors in search for new physics, *Sci. China Phys. Mech. Astron.* **68**, 249512 (2025), arXiv:2410.04340 [gr-qc].

[37] Y. Hu, P.-P. Wang, Y.-J. Tan, and C.-G. Shao, Universal calculation approach of overlap reduction function for pulsar timing array and laser interferometer detector, *Phys. Rev. D* **111**, 084065 (2025).

[38] Y. Hu, P.-P. Wang, Y.-J. Tan, and C.-G. Shao, Full analytic expression of overlap reduction function for gravitational wave background with pulsar timing arrays, *Phys. Rev. D* **106**, 024005 (2022), arXiv:2205.09272 [gr-qc].

[39] R. w. Hellings and G. s. Downs, UPPER LIMITS ON THE ISOTROPIC GRAVITATIONAL RADIATION BACKGROUND FROM PULSAR TIMING ANALYSIS, *Astrophys. J. Lett.* **265**, L39 (1983).

[40] S. V. Dhurandhar, K. Rajesh Nayak, S. Koshti, and J. Y. Vinet, Fundamentals of the LISA stable flight formation, *Class. Quant. Grav.* **22**, 481 (2005), arXiv:gr-qc/0410093.

[41] N. J. Cornish and S. L. Larson, Space missions to detect the cosmic gravitational wave background, *Class. Quant. Grav.* **18**, 3473 (2001), arXiv:gr-qc/0103075.

[42] T. Robson, N. J. Cornish, and C. Liu, The construction and use of LISA sensitivity curves, *Class. Quant. Grav.* **36**, 105011 (2019), arXiv:1803.01944 [astro-ph.HE].

[43] Z. Luo, Y. Wang, Y. Wu, W. Hu, and G. Jin, The Taiji program: A concise overview, *PTEP* **2021**, 05A108 (2021).

[44] H. Jiang, B. Xu, and Y.-L. Zhang, Artificial Precision Polarization Array: Sensitivity for the axion-like dark matter with clock satellites, (2025), arXiv:2511.04400 [astro-ph.CO].

[45] Y.-Y. Liu, J.-R. Zhang, M.-H. Du, H.-S. Liu, P. Xu, and Y.-L. Zhang, Detectability of axion-like dark matter for different time-delay interferometry combinations in space-based gravitational wave detectors, (2025), arXiv:2511.15438 [gr-qc].